Biomedical Optics EXPRESS

Cornea characterization using a combined multiphoton microscopy and optical coherence tomography system

Tom Lai and Shuo Tang*

Department of Electrical and Computer Engineering, University of British Columbia, 2332 Main Mall, Vancouver, BC, V6T 1Z4, Canada
**tang@ece.ubc.ca*

Abstract: We present a multimodal imaging system which combines multiphoton microscopy and optical coherence tomography to visualize the morphological structures, and to quantify the refractive index (RI) and thickness of cornea. The morphological similarities and differences at different corneal layers across various species are identified. In the piscine and human corneas, the stromata exhibit thin fibers that indicate an overall collagen direction. Human corneas display collagen micro-folds which cause increased light attenuation. In the murine, porcine and bovine corneas, the stromata show interwoven collagen patterns. The Bowman's layer and the Descemet's membrane are also distinguished in some species. The RI and thicknesses are quantified for the epithelium and the stromal layers respectively, where the epithelium is found to have slightly higher RI than the stroma. The average epithelial and stromal RI are, respectively, 1.371 ± 0.016 and 1.360 ± 0.008 for the murine corneas; 1.502 ± 0.057 and 1.335 ± 0.011 for the piscine corneas; 1.433 ± 0.023 and 1.357 ± 0.013 for the human corneas; 1.476 ± 0.091 and 1.343 ± 0.013 for the porcine corneas; and 1.400 ± 0.007 and 1.376 ± 0.003 for the bovine corneas. The multimodal system can potentially provide a comprehensive characterization of the cornea.

OCIS codes: (180.4315) Nonlinear microscopy; (110.4500) Optical coherence tomography.

References and links

1. D. W. DelMonte and T. Kim, "Anatomy and physiology of the cornea," J. Cataract Refract. Surg. **37**(3), 588–598 (2011).
2. R. F. Guthoff, A. Zhivov, and O. Stachs, "In vivo confocal microscopy, an inner vision of the cornea - a major review," Clin. Experiment. Ophthalmol. **37**(1), 100–117 (2009).
3. M. D. Merindano, J. Costa, M. Canals, J. M. Potau, and D. Ruano, "A comparative study of Bowman's layer in some mammals: relationships with other constituent corneal structures," Eur. J. Anat. **6**(3), 133–139 (2002).
4. K. M. Meek and A. J. Quantock, "The use of x-ray scattering techniques to determine corneal ultrastructure," Prog. Retin. Eye Res. **20**(1), 95–137 (2001).
5. Y. L. Kim, J. T. Walsh, Jr., T. K. Goldstick, and M. R. Glucksberg, "Variation of corneal refractive index with hydration," Phys. Med. Biol. **49**(5), 859–868 (2004).
6. F. Aptel, N. Olivier, A. Deniset-Besseau, J. M. Legeais, K. Plamann, M. C. Schanne-Klein, and E. Beaurepaire, "Multimodal nonlinear imaging of the human cornea," Invest. Ophthalmol. Vis. Sci. **51**(5), 2459–2465 (2010).
7. B. R. Masters, "Correlation of histology and linear and nonlinear microscopy of the living human cornea," J. Biophotonics **2**(3), 127–139 (2009).
8. N. Efron, I. Perez-Gomez, H. A. Mutalib, and J. Hollingsworth, "Confocal microscopy of the normal human cornea," Cont. Lens Anterior Eye **24**(1), 16–24 (2001).
9. W. R. Zipfel, R. M. Williams, and W. W. Webb, "Nonlinear magic: multiphoton microscopy in the biosciences," Nat. Biotechnol. **21**(11), 1369–1377 (2003).
10. S. Tang, Y. Zhou, K. K. H. Chan, and T. Lai, "Multiscale multimodal imaging with multiphoton microscopy and optical coherence tomography," Opt. Lett. **36**(24), 4800–4802 (2011).
11. Y. Zhou, K. K. H. Chan, T. Lai, and S. Tang, "Characterizing refractive index and thickness of biological tissues using combined multiphoton microscopy and optical coherence tomography," Biomed. Opt. Express **4**(1), 38–50 (2013).

#205348 - $15.00 USD Received 28 Jan 2014; revised 30 Mar 2014; accepted 4 Apr 2014; published 14 Apr 2014

12. R. LaComb, O. Nadiarnykh, S. S. Townsend, and P. J. Campagnola, "Phase matching considerations in second harmonic generation from tissues: effects on emission directionality, conversion efficiency and observed morphology," Opt. Commun. **281**(7), 1823–1832 (2008).
13. R. M. Williams, W. R. Zipfel, and W. W. Webb, "Interpreting second-harmonic generation images of collagen I fibrils," Biophys. J. **88**(2), 1377–1386 (2005).
14. J. M. Bueno, E. J. Gualda, and P. Artal, "Analysis of corneal stroma organization with wavefront optimized nonlinear microscopy," Cornea **30**(6), 692–701 (2011).
15. B. J. Kaluzny, J. J. Kałuzny, A. Szkulmowska, I. Gorczyńska, M. Szkulmowski, T. Bajraszewski, M. Wojtkowski, and P. Targowski, "Spectral optical coherence tomography: a novel technique for cornea imaging," Cornea **25**(8), 960–965 (2006).
16. S. Shah, A. Chatterjee, M. Mathai, S. P. Kelly, J. Kwartz, D. Henson, and D. McLeod, "Relationship between corneal thickness and measured intraocular pressure in a general ophthalmology clinic," Ophthalmology **106**(11), 2154–2160 (1999).
17. S. R. Uhlhorn, F. Manns, H. Tahi, P. Rol, and J. M. Parel, "Corneal group refractive index measurement using low-coherence interferometry," Proc. SPIE **3246**, 14–21 (2003).
18. J. W. McLaren, C. B. Nau, J. C. Erie, and W. M. Bourne, "Corneal thickness measurement by confocal microscopy, ultrasound, and scanning slit methods," Am. J. Ophthalmol. **137**(6), 1011–1020 (2004).
19. M. Bechmann, M. J. Thiel, A. S. Neubauer, S. Ullrich, K. Ludwig, K. R. Kenyon, and M. W. Ulbig, "Central corneal thickness measurement with a retinal optical coherence tomography device versus standard ultrasonic pachymetry," Cornea **20**(1), 50–54 (2001).
20. C. Wirbelauer and D. T. Pham, "Continuous monitoring of corneal thickness changes during LASIK with online optical coherence pachymetry," J. Cataract Refract. Surg. **30**(12), 2559–2568 (2004).
21. Y. Barkana, Y. Gerber, U. Elbaz, S. Schwartz, G. Ken-Dror, I. Avni, and D. Zadok, "Central corneal thickness measurement with the pentacam Scheimpflug system, optical low-coherence reflectometry pachymeter, and ultrasound pachymetry," J. Cataract Refract. Surg. **31**(9), 1729–1735 (2005).
22. A. Faramarzi and H. Ziai, "Central corneal thickness measurement by ultrasound versus Orbscan II," J Ophthalmic Vis Res **3**(2), 83–86 (2008).
23. B. Vasudevan, T. L. Simpson, and J. G. Sivak, "Regional variation in the refractive-index of the bovine and human cornea," Optom. Vis. Sci. **85**(10), 977–981 (2008).
24. K. D. Rao, Y. Verma, H. S. Patel, and P. K. Gupta, "Non-invasive ophthalmic imaging of adult zebrafish eye using optical coherence tomography," Curr. Sci. **90**(11), 1506–1510 (2006).
25. G. J. Tearney, M. E. Brezinski, J. F. Southern, B. E. Bouma, M. R. Hee, and J. G. Fujimoto, "Determination of the refractive index of highly scattering human tissue by optical coherence tomography," Opt. Lett. **20**(21), 2258–2260 (1995).
26. N. Morishige, A. J. Wahlert, M. C. Kenney, D. J. Brown, K. Kawamoto, T. Chikama, T. Nishida, and J. V. Jester, "Second-harmonic imaging microscopy of normal human and keratoconus cornea," Invest. Ophthalmol. Vis. Sci. **48**(3), 1087–1094 (2007).
27. N. Morishige, W. M. Petroll, T. Nishida, M. C. Kenney, and J. V. Jester, "Noninvasive corneal stromal collagen imaging using two-photon-generated second-harmonic signals," J. Cataract Refract. Surg. **32**(11), 1784–1791 (2006).
28. G. Latour, I. Gusachenko, L. Kowalczuk, I. Lamarre, and M. C. Schanne-Klein, "In vivo structural imaging of the cornea by polarization-resolved second harmonic microscopy," Biomed. Opt. Express **3**(1), 1–15 (2012).
29. S. Hayashi, T. Osawa, and K. Tohyama, "Comparative observations on corneas, with special reference to Bowman's layer and Descemet's membrane in mammals and amphibians," J. Morphol. **254**(3), 247–258 (2002).
30. S. Patel, J. Marshall, and F. W. Fitzke, "Refractive index of the human corneal epithelium and stroma," J. Refract. Surg. **11**(2), 100–105 (1995).
31. L. R. Nelson, D. O. Hodge, and W. M. Bourne, "In vitro comparison of Chen medium and Optisol-GS medium for human corneal storage," Cornea **19**(6), 782–787 (2000).
32. S. Patel, J. L. Alió, and J. J. Pérez-Santonja, "Refractive index change in bovine and human corneal stroma before and after LASIK: a study of untreated and re-treated corneas implicating stromal hydration," Invest. Ophthalmol. Vis. Sci. **45**(10), 3523–3530 (2004).

1. Introduction

Cornea consists of five basic layers: epithelium, Bowman's layer, stroma, Descemet's membrane, and endothelium [1,2]. The epithelium is the outermost region of the cornea, which consists of superficial polygonal cells, winged cells and basal columnar cells. The epithelium serves as the mechanical barrier to dust, fluids and bacteria. Directly beneath the epithelium is the Bowman's layer which is composed of a condensed layer of randomly arranged collagen fiber bundles [2,3]. These fiber bundles are finer than, but continuous with, the collagen fiber bundles found in the stroma. The compact arrangement of these collagen fiber bundles provides mechanical strength and helps the cornea maintain its shape. However, not all species have a Bowman's layer [3]. Below the Bowman's layer is the stroma. It is the thickest layer of the cornea and is composed of mainly type-I collagen fibers arranged in lamellae [1,4]. These fibers have uniform diameters of 25-45 nm and are regularly arranged

#205348 - $15.00 USD Received 28 Jan 2014; revised 30 Mar 2014; accepted 4 Apr 2014; published 14 Apr 2014

with respect to each other. This highly organized collagen network contributes to the transparency of the cornea [5]. The collagen arrangement also provides the cornea its rigidity and form. Underneath the stroma is the Descemet's membrane which is a basement membrane made of a thin sheet of collagen. It is composed of primarily type-IV collagen and non-collagenous components such as fibronectin, laminin, and elastin [1,6]. As the innermost layer of the cornea, the endothelium keeps the stroma in a deturgesced state through a process of pumping and leaking fluids into and out of the stroma. Without this pumping action, the stroma would swell up and the cornea would become translucent or opaque [5]. The endothelium is composed of a thin, monolayer of cells which forms a honeycomb mosaic.

Visualization of the corneal morphology is useful in many ophthalmology applications, such as: analyzing the effects of contact lens wear and topical medications; identifying the type of infectious keratitis; and observing corneal ulcers, keratoconus, and the wound healing process [2,7]. The most common methods for corneal imaging include confocal microscopy (CM), multiphoton microscopy (MPM), and optical coherence tomography (OCT).

CM uses a light beam that passes through a source pinhole and an objective lens to illuminate the sample [2,7]. The reflected light returns through the objective lens and enters a photo-detector via a detection pinhole. The detection pinhole blocks the out-of-focus light and allows CM to have subcellular resolution and optical sectioning capability. CM has been used for *in vivo* imaging of the corneal morphology. However, it is limited to viewing cellular structures and nerves since it cannot see collagen well [8]. Also, it cannot visualize the Bowman's layer or the Descemet's membrane effectively.

MPM is a nonlinear imaging technique that has subcellular resolution, deep penetration and optical sectioning capability [9]. MPM uses multiple photons of lower energy to create an excitation normally produced by the absorption of a single photon of higher energy [10]. MPM can detect two-photon excited fluorescence (TPEF) and second harmonic generation (SHG). TPEF signal comes from intrinsic sources such as nicotinamide adenine dinucleotide phosphate (NADH) and elastin. SHG signal comes from non-centrosymmetric molecules such as collagen [11]. MPM can be used to observe cells based on the autofluorescence from NADH and collagen morphology based on the SHG contrast. For imaging thick tissues, backward detection configuration is typical needed. Several theories such as quasi phase-matching and hollow rods in collagen fibers have been proposed to explain the mechanism for backward SHG [12,13]. The primary drawbacks of MPM are its slow acquisition speed and small field of view. Aptel et al. used MPM to image the entire thickness of the human cornea [6]. They were able to identify the 5 corneal layers using a combination of TPEF, forward-scattered SHG, backward-scattered SHG, and third harmonic generation. Bueno et al. used MPM to compare stromal collagen structures between human, porcine, bovine, rabbit, rat, and chicken corneas [14]. However, they did not identify the cellular layers or the Descemet's membrane.

OCT is based on the interferometry technique [11,15]. It provides cross-sectional view of the tissue by detecting the interference between the reflected light from a sample arm and a reference arm. OCT can identify structural properties in the cornea such as scars, foreign objects, superficial pathologies, irregular thicknesses, and epithelial and Descemet's membrane detachments [15]. The main disadvantages of OCT are its lack of biochemical specificity and cellular level resolution.

In addition to the morphological visualization, the ability to quantitatively characterize the corneal thickness and RI is also of great importance in ophthalmology [5,11,16,17]. The measurement of the corneal thickness is needed in many clinical situations, such as the diagnosis of corneal degeneration, endothelial dysfunction, and stromal dystrophy. The measurement of the corneal RI is important for laser refractive surgery. The thickness and the RI of the cornea are also used as indicators for corneal hydration and intraocular pressure. A constant corneal hydration is necessary for the maintenance of its transparency. When the balance is disrupted, the cornea swells resulting in regions of varying RI, which causes the cornea to become cloudy and translucent. The intraocular pressure is an important parameter in the diagnosis and treatment of glaucoma.

#205348 - $15.00 USD Received 28 Jan 2014; revised 30 Mar 2014; accepted 4 Apr 2014; published 14 Apr 2014

Corneal thickness can be measured using CM, OCT, or ultrasound. CM examines the cornea by optically advancing through the entire cornea. By identifying the corneal boundaries, the thickness can be determined [18]. However, due to refraction, this method needs to be calibrated by examining a series of contact lenses with known thicknesses. There are many clinical devices to measure corneal thickness using OCT. However these devices need to assume a corneal group index in their calculations [19,20]. Ultrasound is the most common method clinically to measure corneal thickness [21]. It requires contact with the subject which may displace the tear film by 7-40 μm or lead to infections [22]. Ultrasound uses an estimated value for the acoustic velocity which can differ between different devices and manufacturers.

RI can be measured using critical angle and OCT techniques. In a handheld refractometer, the incidence angle is tuned until the critical angle is reached, from which the RI can be measured [23]. However, it can only measure the RI of the medium which is in direct contact with the optics. It cannot measure multilayered samples. Focus tracking using OCT has been reported for noninvasive RI measurements in tissues [24,25]. RI can be obtained by tracking the focus shift resulting from translating the focus of an objective along the optical axis within a medium. Rao et al. used the focus tracking method to estimate the RI of the zebrafish lens [24]. However, determining the front and rear surfaces of a multilayered biological sample by OCT can be difficult.

In this paper, we present a combined MPM and OCT system to image corneal morphology for five different species: mouse, fish, human, pig, and cow. In the OCT images, a full cross-sectional view of the cornea over a large field of view can be captured at fast speed. The OCT images are able to identify the different structural layers, such as the epithelium and the stroma, using the scattering contrast. In addition, the co-registered MPM images can identify the cellular and collagen fiber structures with high resolution at different depths of the cornea using biochemically specific TPEF and SHG contrasts. The five corneal layers can be distinguished. Furthermore, the thickness and the RI of the epithelium and the stroma can be calculated from the co-registered MPM and OCT images. The multimodal system has several advantages over existing methods. It provides both imaging and quantitative characterization of the cornea. This allows researchers and doctors to obtain more information for a more reliable analysis. It can be used to characterize biological tissues with multiple layers. Finally, it is label-free and requires no sample preparation which makes it possible to be implemented *in vivo*.

2. System design

The imaging system utilized in this study is shown in Fig. 1. A detailed description of the system can be found in our previous work [10]. A sub-10 fs Ti: Sapphire laser (Fusion PRO 400, Femtolasers) with a centre-wavelength of 800 nm, a bandwidth of 120 nm and a coherence length of 2.3 μm in air is used as the light source for both the MPM and the OCT imaging. The laser light passes through a prism-based dispersion pre-compensation unit before entering a 50/50 beam splitter. The beam splitter divides the light into a sample beam and a reference beam. For MPM imaging, the sample beam illuminates the sample through a 40 × water immersion objective lens (LUMPlanFL N, Olympus) with numerical aperture (NA) of 0.8, and excites both the TPEF and SHG signals. The two signals are separated by a dichroic mirror and are directed to their respective photomultiplier tubes (PMTs). A piezo-scanner and two galvanometer mirrors are used to achieve axial and transversal scanning, respectively. For OCT imaging, the backscattered beam from the sample combines with that from the reference mirror through the beam splitter into the spectrometer. The spectrometer is composed of a diffraction grating, a compound lens, and a line CCD camera. A dispersion balancing unit is added in the reference arm to compensate for dispersion effects. Here, it should be noticed that two different objectives and compound lenses are selectively utilized for OCT imaging depending on the sample thickness. For the murine and piscine corneas, a 10 × objective (MPlanFL N, Olympus, NA = 0.3) and an effective f = 37.5 mm lens in the spectrometer are used. For thicker samples such as the human, porcine and bovine corneas, a

#205348 - $15.00 USD Received 28 Jan 2014; revised 30 Mar 2014; accepted 4 Apr 2014; published 14 Apr 2014

4 × objective (Plan N, Olympus, NA = 0.1) and an effective f = 100 mm lens in the spectrometer are used.

The MPM axial and lateral resolutions are ~1.5 μm and ~0.6 μm, respectively, for the 40 × objective lens [11]. The OCT lateral resolution is dependent on the NA of the objective lens while the axial resolution is dependent on the coherence length of the laser source and the spectrometer design. The OCT axial and lateral resolutions for the 10 × objective lens with the f = 37.5 mm spectrometer configuration are ~2.8 μm and ~2 μm, respectively [11]. The OCT axial and lateral resolutions for the 4 × objective lens with the f = 100 mm spectrometer configuration are ~3.4 μm and ~5.4 μm, respectively. The MPM and OCT frame rates are ~0.4 and ~100 frames per second, respectively [11].

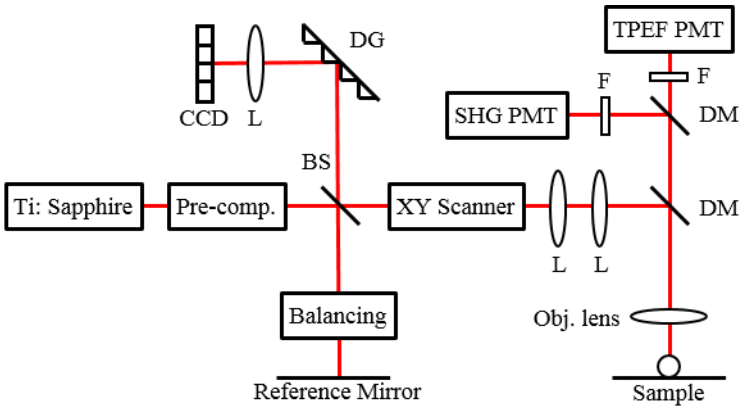

Fig. 1. Experimental setup of the combined MPM/OCT imaging system. L: lens; DG: diffraction grating; BS: beam splitter; PMT: photomultiplier tube; F: filter; DM: dichroic mirror.

3. Method

3.1 Preparation of corneal tissues

Murine and piscine eyeballs are obtained from C3H/HeN mice and tilapia fish, respectively. Porcine and bovine eyeballs are acquired from the animal facilities on campus and a local farm, respectively. The eyeballs are positioned inside a container with the anterior side facing the laser source. They are submerged under BSS sterile irrigation solution (Alcon Canada Inc.), and the corneas are imaged from the anterior side to the posterior side. The murine, piscine, and bovine eyeballs are imaged within 6 hours post-mortem. The porcine eyeballs are imaged within 12 hours post-mortem.

Human corneas are obtained from the local eye bank. They are determined to be unsuitable for transplantation and thus are released for research purposes. The human corneas are excised corneal tissues. The samples are positioned inside a container with the laser source entering the posterior side first. These corneas are submerged under Optisol corneal storage media (Bausch & Lomb), and then imaged. They are stored in Optisol and are imaged within 6 weeks post-mortem. Unlike the other samples, the human corneas are several weeks old prior to imaging and exhibit some cloudiness, which limit the laser penetration through the thicker cellular layer of the epithelium. Therefore, in order to image the full thickness in MPM, the corneas are imaged with the laser entering the thinner cellular layer of the endothelium.

The purpose of the study is approved by the ethics committee of the University of British Columbia.

#205348 - $15.00 USD Received 28 Jan 2014; revised 30 Mar 2014; accepted 4 Apr 2014; published 14 Apr 2014

3.2 MPM/OCT imaging and RI and thickness measurement

OCT cross-sectional image of the sample (e.g. Fig. 2(a)) is taken with the 10 × or the 4 × objective lens depending on the sample thickness. The OCT axial imaging depth, determined by the effective focal length of the lens in the spectrometer, is ~550 μm for murine and piscine imaging and ~1500 μm for human, porcine, and bovine imaging. For MPM imaging, the objective lens is switched to the 40 × without moving the sample. By stepping the objective lens with the piezo-scanner, a stack of MPM *en face* images are obtained. By reconstructing a 3D volume using the *en face* images, a MPM cross-sectional image is generated (e.g. Fig. 2(b)). The dimension of the MPM cross-sectional image in the depth direction is determined by the number of frames and the step size of the image stack. The maximum scanning range of the piezo-scanner is 400 μm. If the sample thickness exceeds this value, multiple overlapping image stacks are taken by adjusting the sample stage with a micrometer. These overlapping MPM stacks are then merged together to form a single 3D volume.

The thickness measured from the OCT image is the sample's optical pathlength, L_p. Assuming the group index is equivalent to the RI, for a sample of thickness t and RI of n, L_p can be expressed as:

$$L_p = t \times n \tag{1}$$

The thickness measured from the MPM cross-sectional image is named optical thickness, L_o, which corresponds to the distance the objective lens is moved when it steps through the sample. Based on multilayer refractions, L_o can be expressed as:

$$L_o = t \times \sqrt{\frac{n_o^2 - (NA)^2}{n^2 - (NA)^2}} \tag{2}$$

where NA is the numeric aperture of the objective lens (40 × , NA = 0.8), and n_0 is the RI of the immersion medium (distilled water, $n_0 = 1.333$).

Therefore, by measuring the thicknesses in the OCT and MPM images respectively, the RI and the physical thickness of the sample can be obtained as [11]:

$$n = \sqrt{\frac{(NA)^2 + \sqrt{(NA)^4 + 4[n_o^2 - (NA)^2]L_p^2 / L_o^2}}{2}} \tag{3}$$

$$t = \frac{\sqrt{2}L_p}{\sqrt{(NA)^2 + \sqrt{(NA)^4 + 4[n_o^2 - (NA)^2]L_p^2 / L_o^2}}} \tag{4}$$

4. Results

4.1 MPM and OCT imaging results

4.1.1 Murine cornea

Figure 2 shows the OCT and MPM images of a murine cornea. The OCT and MPM cross-sectional images are shown in Figs. 2(a) and 2(b), respectively. In the OCT cross-sectional image, two corneal layers are clearly distinguished. The top layer, L1, corresponds to the epithelium while the bottom layer, L2, is composed of mainly the stroma. The boundary between the epithelial and the stromal layers is observed due to the change in the RI at the interface. Collagen laminae can be seen in the stromal region in the OCT image. However, the thin Bowman's layer, Descemet's membrane, and endothelium cannot be differentiated from the stroma due to the lack of axial resolution and specificity in OCT. In the MPM cross-sectional image, three layers are clearly observed through the TPEF and SHG contrasts, color coded in red and green, respectively. Color yellow represents areas with overlapping TPEF

#205348 - $15.00 USD Received 28 Jan 2014; revised 30 Mar 2014; accepted 4 Apr 2014; published 14 Apr 2014

and SHG signals which are caused by cross-talk between the two channels. From the top, the first layer (red) is the epithelium. The strong TPEF signal comes from the NADH inside the epithelial cells. The second layer (green) corresponds to the thick stroma which has strong SHG signals due to the type-I collagen fibers. The thin Bowman's layer is not differentiable from the stroma. The third layer (red) is composed of the Descemet's membrane and the monolayer of endothelial cells. They provide TPEF contrast from elastin in the Descemet's membrane and NADH in the endothelial cells. The co-registered MPM imaging area is marked by the red dashed rectangle on the larger-scaled OCT image in Fig. 2(a).

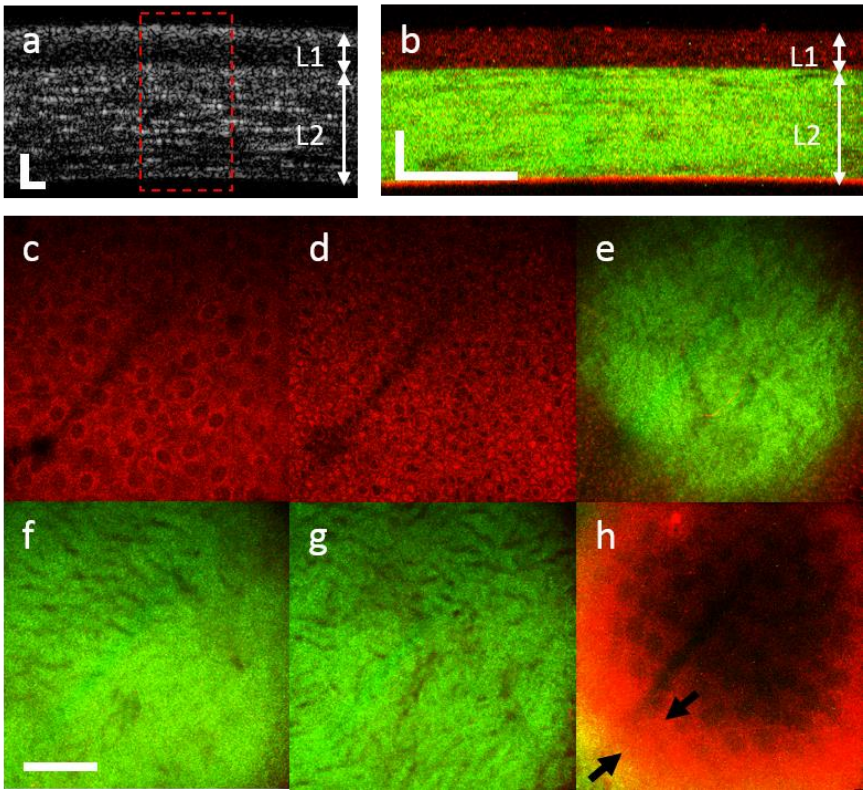

Fig. 2. OCT and MPM images of a murine cornea. (a) OCT cross-sectional image. (b) MPM cross-sectional image. L1 is the epithelium layer. L2 is the Bowman's layer, stroma, Descemet's membrane, and endothelium layers. (c) – (h) MPM *en face* images. (c) Anterior epithelium. (d) Posterior epithelium. (e) Junction between the epithelium and the stroma. (f) Anterior stroma. (g) Posterior stroma. (h) Descemet's membrane and Endothelium. Arrowheads point to the Descemet's membrane. (c) – (h) are 12 µm, 28 µm, 42 µm, 92 µm, 146 µm, and 160 µm below the surface of the cornea, respectively. TPEF signals are in red. SHG signals are in green. Scale bars are 50 µm. The red dashed rectangle in the OCT image marks the co-registered MPM imaging area.

The MPM *en face* images from the anterior side to the posterior side of the murine cornea are shown in Figs. 2(c)-2(h). Larger cells are observed near the anterior side of the epithelium in Fig. 2(c) while smaller cells are observed at the posterior side of the epithelium in Fig. 2(d). Figure 2(e) shows the junction between the epithelium and the stroma. Interwoven collagen structures are observed in the stromal layer in Figs. 2(f) and 2(g). A single layer of endothelium cells arranged in a honeycomb mosaic is detected at the posterior end of the cornea as shown in Fig. 2(h). The Descemet's membrane is the region between the posterior stroma and the endothelial layer. This membrane is composed of mostly type-IV collagen which cannot be observed by SHG. However, it also contains elastin which provides TPEF contrast [6]. It is identified as the region between the arrowheads in Fig. 2(h) where there is

#205348 - $15.00 USD Received 28 Jan 2014; revised 30 Mar 2014; accepted 4 Apr 2014; published 14 Apr 2014

TPEF contrast but no honeycomb structure of cells. The dark, diagonal band observable in Figs. 2(c), 2(d) and 2(h) is an artifact that may have been caused by a blockage of the beam somewhere in the beam path. A potential solution is to identify and replace the component causing the blockage.

4.1.2 Piscine cornea

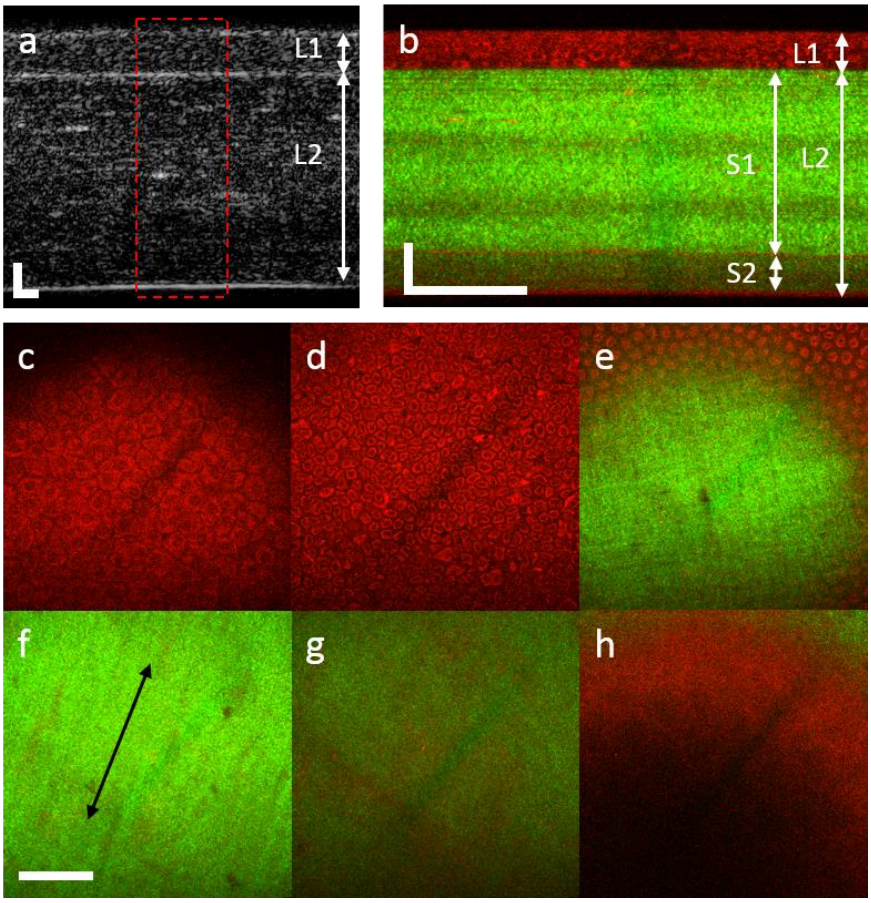

Fig. 3. OCT and MPM images of a piscine cornea. (a) OCT cross-sectional image. (b) MPM cross-sectional image. S1 and S2 are the first and second stromal layers. (c) – (h) MPM *en face* images. (c) Anterior epithelium. (d) Posterior epithelium. (e) Junction between the epithelium and the stroma. (f) Stroma in S1. (g) Stroma in S2. (h) Descemet's membrane and endothelium. (c) – (h) are 4 µm, 28 µm, 44 µm, 69 µm, 253 µm, and 282 µm below the surface of the cornea, respectively. Double arrow marks the direction of the collagen fiber bundles. Scale bars are 50 µm. The red dashed rectangle in the OCT image marks the co-registered MPM imaging area.

OCT and MPM images of a piscine cornea is shown in Fig. 3. The OCT and MPM cross-sectional images are shown in Figs. 3(a) and 3(b), while the MPM *en face* images are shown in Figs. 3(c)-3(h). Similar to the murine cornea, the epithelium, L1, and the stroma, L2, are identified in both the OCT and the MPM cross-sectional images. However, in the MPM cross-sectional image, the stroma can be further differentiated into two distinct sub-layers with different SHG intensities, labeled as S1 and S2. In the *en face* images, larger cells are detected near the anterior side of the epithelium in Fig. 3(c) while smaller cells are observed at the posterior side of the epithelium in Fig. 3(d). The interface between the epithelium and the stroma is shown in Fig. 3(e). Figures 3(f) and 3(g) show representative collagen structures

#205348 - $15.00 USD Received 28 Jan 2014; revised 30 Mar 2014; accepted 4 Apr 2014; published 14 Apr 2014

in the two stromal layers, S1 and S2, respectively. In the S1 layer, collagen fibers appear to form an orientation as marked by the black double arrow. This orientation changes direction from lamella to lamella. Meanwhile, the collagen fibers within the S2 layer appear to be finer. Due to the difference in the fiber sizes, S1 shows a much higher SHG signal intensity than S2. Lastly, a thin layer of TPEF signal composed of the Descemet's membrane and the endothelium is seen at the posterior end of the cornea, as shown in Fig. 3(h).

4.1.3 Human cornea

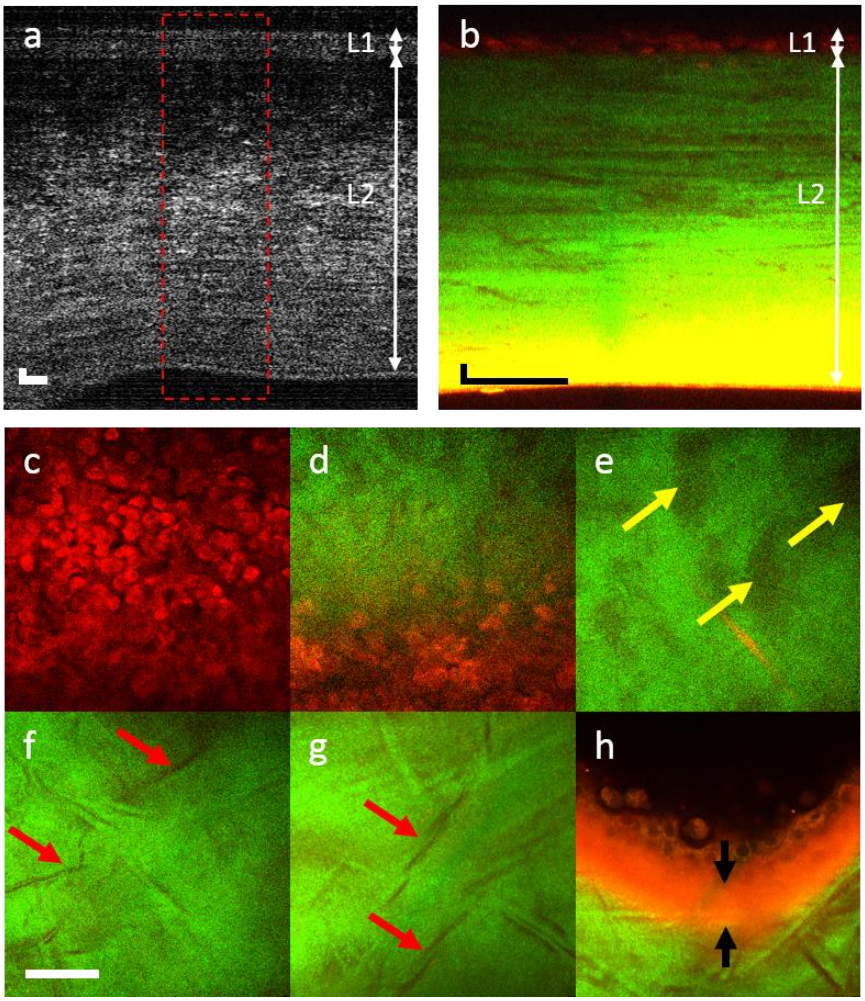

Fig. 4. OCT and MPM images of a human cornea. (a) OCT cross-sectional image. (b) MPM cross-sectional image. (c) – (h) MPM *en face* images. (c) Epithelium. (d) Bowman's layer. (e) – (g) Anterior to posterior stroma. (h) Descemet's membrane and endothelium. Yellow arrowheads point to regions of weaker SHG signal in the anterior stroma. Red arrowheads point to collagen micro-folds. Black arrowheads point to the Descemet's membrane. (c) – (h) are 42 µm, 68 µm, 110 µm, 340 µm, 680 µm, and 870 µm below the surface of the cornea, respectively. Scale bars are 50 µm. The red dashed rectangle in the OCT image marks the co-registered MPM imaging area.

Figure 4 shows the OCT and MPM images of a human cornea. The OCT and MPM cross-sectional images are shown in Figs. 4(a) and 4(b), and the MPM *en face* images are shown in Figs. 4(c)-4(h). Although the human corneas are imaged with the laser entering the cornea from the posterior side, the images in Fig. 4 have been rearranged such that the orientation

#205348 - $15.00 USD Received 28 Jan 2014; revised 30 Mar 2014; accepted 4 Apr 2014; published 14 Apr 2014

matches the format for the other species. Both the epithelial and stromal layers are observed in the OCT and MPM cross-sectional images. Because the human cornea attenuates the laser power significantly, the TPEF contrast is increased post-process to visualize the epithelium in Fig. 4(b). As such, the increased TPEF signal overlaps with the strong SHG signal at the posterior stroma to cause the bright yellow color in the image. The cellular structure of the epithelium is shown in Fig. 4(c) while the transition between the epithelium and the stroma is displayed in Fig. 4(d). The SHG signal in Fig. 4(d) is more indistinct and diffused which corresponds to the Bowman's layer. Figure 4(e) shows the anterior stroma just below the Bowman's layer, where it has regions of weak SHG signal as marked by the yellow arrowheads. Such patterns have also been observed by Morishige et al. [26,27]. Similar to the piscine corneas, small collagen fibers are observed that together seem to indicate a general orientation of the overall collagen structure, which varies from lamella to lamella. Furthermore, straight and dark ridges that are not present in the other species are seen in Figs. 4(f) and 4(g), marked with red arrowheads. These dark ridges are suspected to be collagen micro-folds that are caused by corneal swelling [7]. The Descemet's membrane and the endothelium are displayed in Fig. 4(h). The Descemet's membrane is shown as the TPEF region (red) between the posterior stroma and the endothelium, marked between the black arrows.

The Bowman's layer is more clearly observed and differentiated from the rest of the stroma in another human data set as shown in Fig. 5. The epithelium and the junction between epithelium and the stroma are shown in Figs. 5(a) and 5(b). The anterior stroma displayed in Figs. 5(d) and 5(e), is identifiable by its distinct regions of weak SHG signal with fine and randomly arranged collagen bundles. Between the anterior stroma and the epithelium is the Bowman's layer as shown in Fig. 5(c), where the collagen signal is more indistinct and diffused. For qualitative comparison, a typical stromal region is shown in Fig. 5(f).

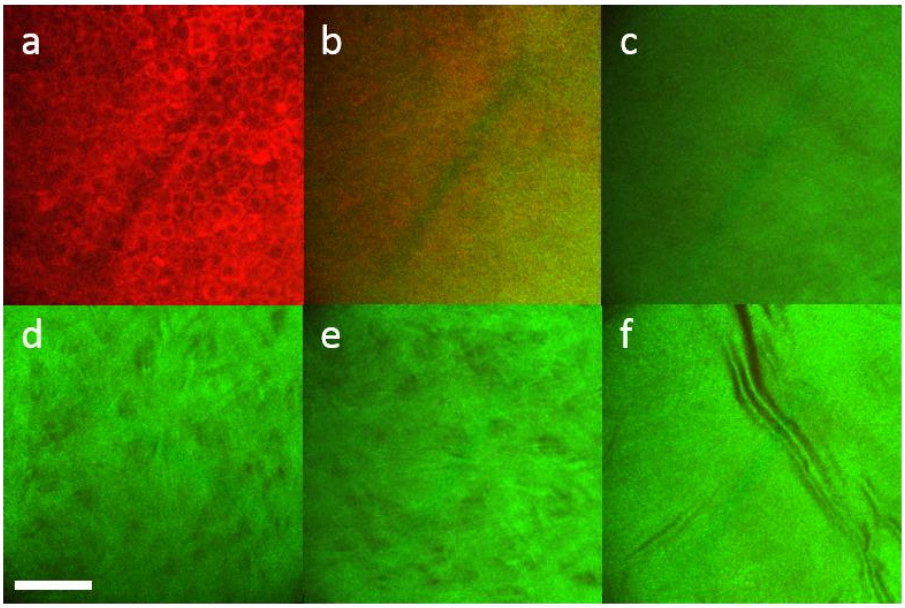

Fig. 5. MPM *en face* images identifying the human Bowman's Layer. (a) Epithelium. (b) Posterior epithelium. (c) Bowman's layer. (d) – (e) Anterior stroma. (f) A typical stromal region. (a) – (f) are 26 µm, 34 µm, 42 µm, 50 µm, 60 µm, and 220 µm below the surface of the cornea, respectively. Scale bar is 50 µm.

#205348 - $15.00 USD Received 28 Jan 2014; revised 30 Mar 2014; accepted 4 Apr 2014; published 14 Apr 2014

4.1.4 Porcine cornea

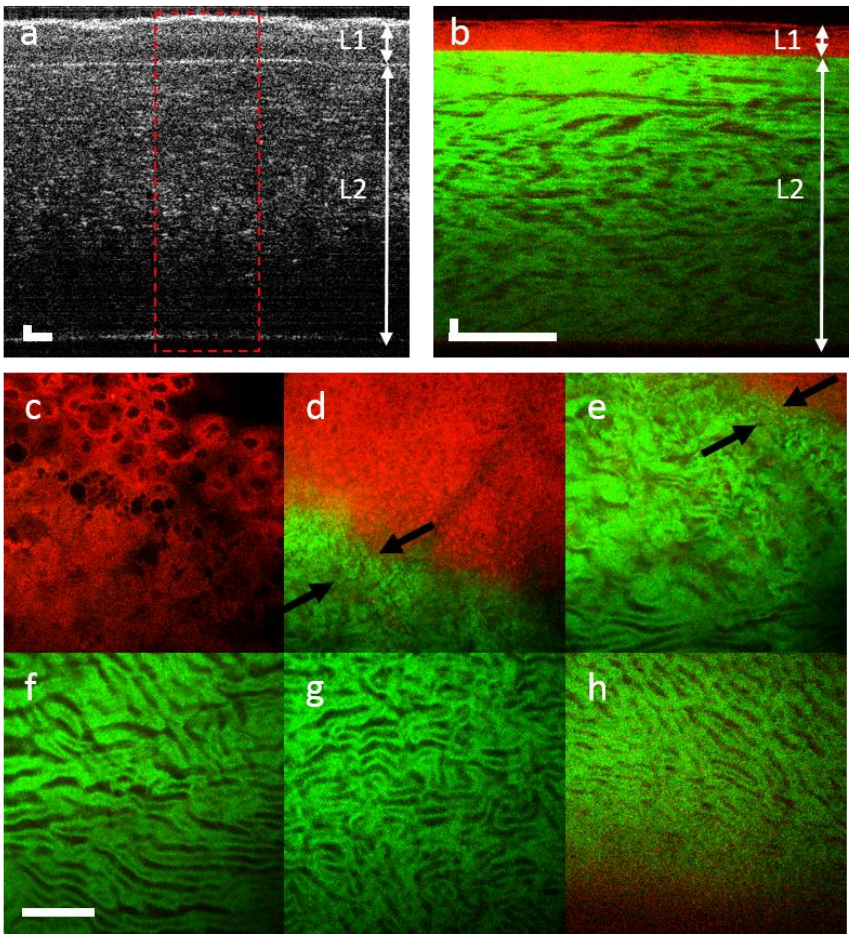

Fig. 6. OCT and MPM images of a porcine cornea. (a) OCT cross-sectional image. (b) MPM cross-sectional image. (c) – (h) MPM *en face* images. (c) Anterior epithelium. (d) – (e) Junction between the posterior epithelium and the stroma. The Bowman's membrane is estimated as the region between the two arrowheads. (f) – (g) Anterior to posterior stroma. (h) Descemet's membrane and endothelium. (c) – (h) are 12 µm, 72 µm, 96 µm, 234 µm, 534 µm, and 772 µm below the surface of the cornea, respectively. Scale bars are 50 µm. The red dashed rectangle in the OCT image marks the co-registered MPM imaging area.

Figure 6 shows the OCT and MPM images of a porcine cornea. The OCT and MPM cross-sectional images are shown in Figs. 6(a) and 6(b), and the MPM *en face* images are shown in Figs. 6(c)-6(h). At the junction between the epithelium and the stroma, finer collagen fiber bundles in a randomly organized pattern are observed in Figs. 6(d) and 6(e), which are specific features of the Bowman's layer. The Bowman's layer is estimated as the region between the arrowheads. The exact boundary for the Bowman's layer is hard to identify due to the smooth transition between the collagen fibers in the Bowman's layer and the collagen fibers in the stroma. The continuous transition from the finer fiber bundles to the larger fiber bundles of the anterior stroma is shown in Fig. 6(e). In the stroma, similar to the murine corneas, interwoven collagen structures are observed (Figs. 6(e)-6(g)). However, different from the murine corneas, large gaps which lack the SHG contrast are observed in both the *en face* and the cross-sectional MPM images. In addition, we notice that the interwoven patterns become finer and denser as we approach the posterior stroma.

#205348 - $15.00 USD Received 28 Jan 2014; revised 30 Mar 2014; accepted 4 Apr 2014; published 14 Apr 2014

The Bowman's layer and its continuous transition into the anterior stroma are better observed in another porcine data set as shown in Fig. 7. The junction between the epithelium and the stroma is shown in Fig. 7(a). The smooth transition of the collagen fiber bundles from finer and more randomly organized to larger and organized is shown in Figs. 7(a) and 7(b). A typical collagen structure seen in the middle of the stroma is shown in Fig. 7(c) for comparison.

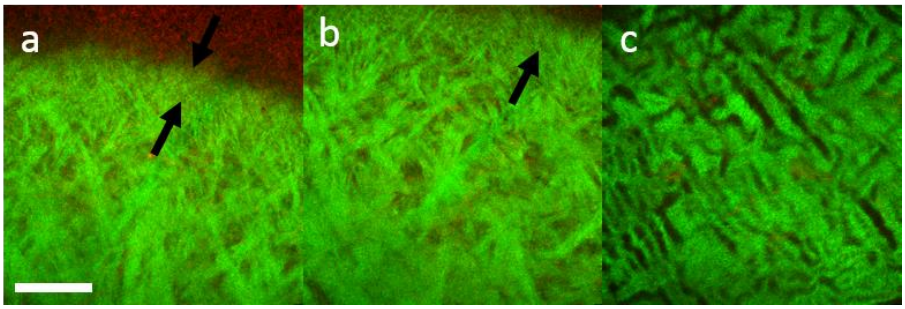

Fig. 7. MPM *en face* images showing collagen structural comparison between the Bowman's layer (a) – (b) and a typical stromal region (c) of a porcine cornea. (a) – (c) are 60 μm, 68 μm, and 190 μm below the surface of the cornea, respectively. Scale bar is 50 μm. The Bowman's membrane is highlighted by the arrowheads.

4.1.5 Bovine cornea

Figure 8 shows the OCT and MPM images of a bovine cornea. The OCT and MPM cross-sectional images are shown in Figs. 8(a) and 8(b), and the MPM *en face* images are shown in Figs. 8(c)-8(k). In Fig. 8(b), dark and bright horizontal lines are observed likely due to the different lamellae in the stroma. In stroma, collagen fibers form lamellae, where the fibers in a particular lamella run parallel with each other, but changes orientation from lamella to lamella. SHG intensity depends on the relative angle between the collagen fiber orientation and the laser polarization [28]. For different fiber orientations, the SHG intensity can vary from maximum to minimum and thus causes the horizontal lines. These lamellae are more clearly observed in the bovine samples likely because they are thicker than in other species. Similar to the porcine corneas, the collagen fibers at the Bowman's layer are finer and in a randomly organized pattern, as shown in Fig. 8(e). The transition from the finer collagen bundles of the Bowman's layer to the larger collagen bundles of the anterior stroma is displayed in Figs. 8(f) and 8(g). In the stroma, similar to the murine and porcine corneas, interwoven collagen structures are identified, as shown in Figs. 8(h) and 8(i). Similar to the porcine cornea, the interwoven patterns become finer and denser towards the posterior stroma. The Descemet's membrane is shown as a cloud of TPEF signals with no distinct structure in Fig. 8(j) while the endothelial cells are shown in Fig. 8(k).

#205348 - $15.00 USD Received 28 Jan 2014; revised 30 Mar 2014; accepted 4 Apr 2014; published 14 Apr 2014

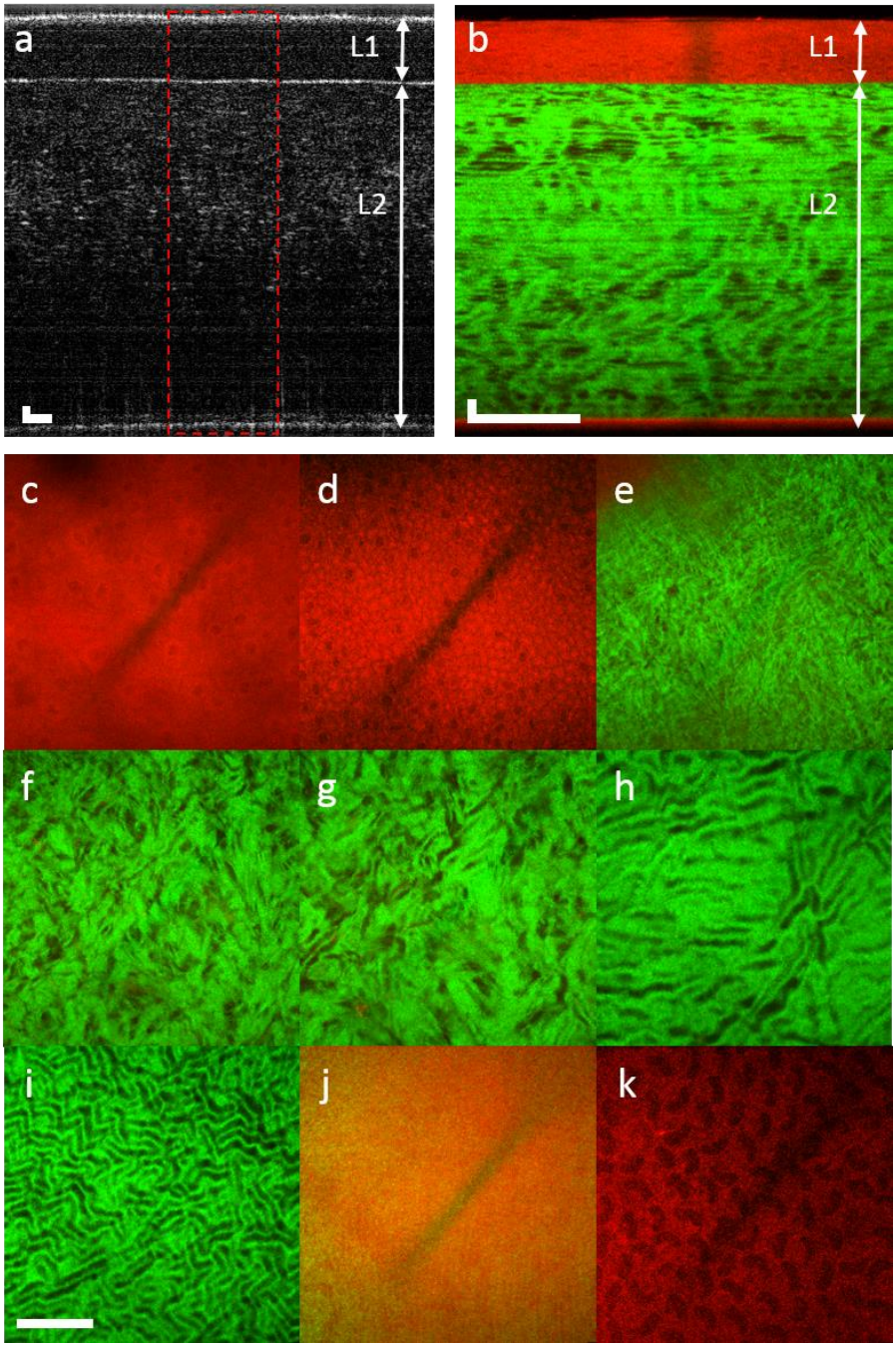

Fig. 8. OCT and MPM images of a bovine cornea. (a) OCT cross-sectional image. (b) MPM cross-sectional image. (c) – (k) MPM *en face* images. (c) Anterior epithelium. (d) Posterior epithelium. (e) Bowman's layer. (f) – (g) Transition from the Bowman's layer to the stroma. (h) Anterior stroma. (i) Posterior stroma. (j) Descemet's membrane. (k) Endothelium. (c) – (k) are 36 µm, 136 µm, 154 µm, 164 µm, 174 µm, 478 µm, 898 µm, 934 µm, and 958 µm below the surface of the cornea, respectively. Scale bars are 50 µm. The red dashed rectangle in the OCT image marks the co-registered MPM imaging area.

#205348 - $15.00 USD Received 28 Jan 2014; revised 30 Mar 2014; accepted 4 Apr 2014; published 14 Apr 2014

4.2 Quantitative characterization

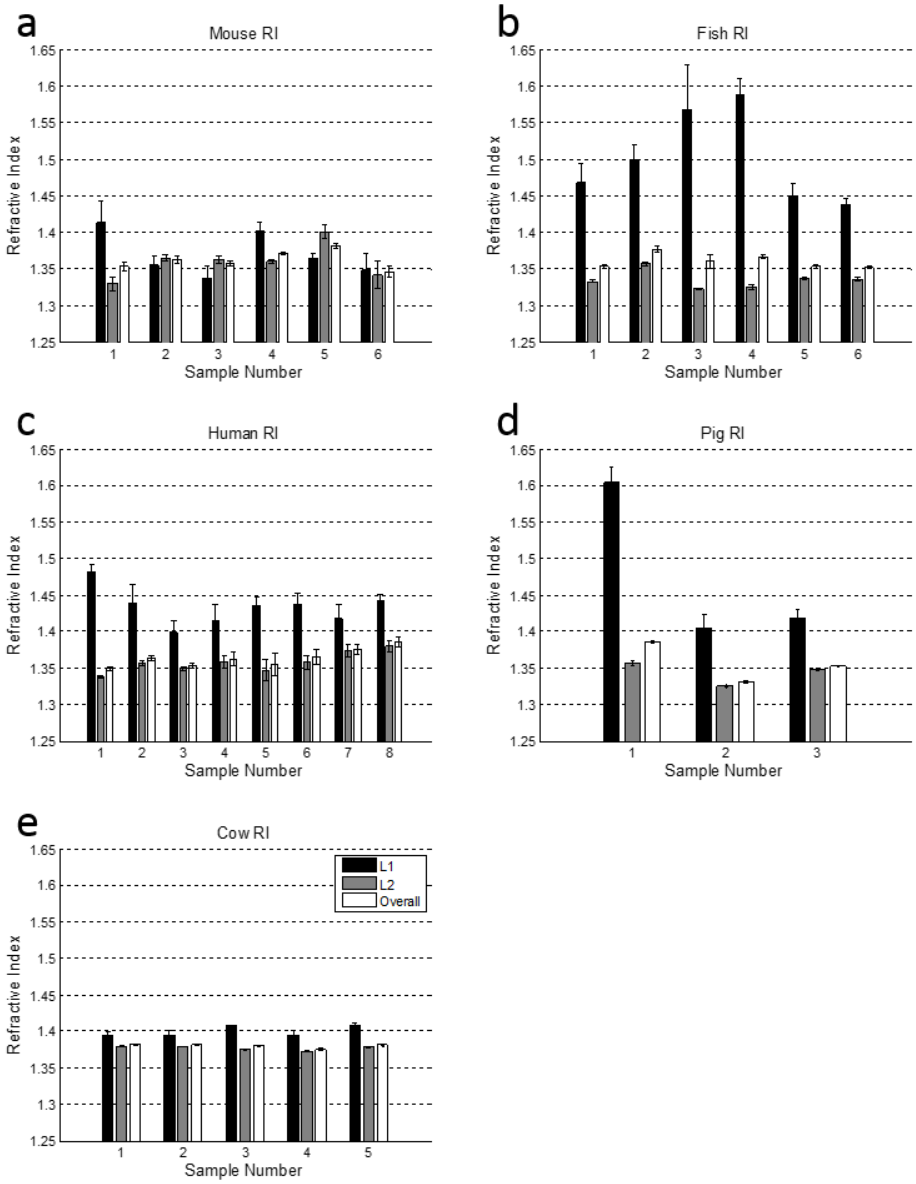

Fig. 9. RI results for 6 murine samples (a), 6 piscine samples (b), 8 human samples (c), 3 porcine samples (d), and 5 bovine samples (e). L1 is epithelium, L2 is the remaining corneal layers, and overall is the entire cornea thickness.

The quantitative characterization of the RI and the thickness of the cornea are carried out on the two distinct layers of the cornea, L1 and L2. The L1 layer corresponds to the epithelium. The L2 layer is mainly composed of stroma but also includes the Descemet's membrane and the endothelium, and the Bowman's layer when it exists. The full thickness of the cornea and the overall RI over the entire cornea thickness are also obtained.

The RI from six murine corneas, five piscine corneas, eight human corneas, three porcine corneas, and five bovine corneas are presented in Figs. 9(a)-9(e), respectively. The RI are calculated by averaging multiple A-lines in the co-registered MPM and OCT cross-sectional

#205348 - $15.00 USD Received 28 Jan 2014; revised 30 Mar 2014; accepted 4 Apr 2014; published 14 Apr 2014

images, where the error bars represent the standard deviations. The RI from the epithelial layer, L1, is found to be higher than the RI from L2 in most of the samples except for a few murine corneas. The epithelial RI is higher likely due to the lipid and DNA compositions in the cell membrane and nuclei. The exception in some of the murine corneas is likely caused by the decrease in measurement accuracy due to the thin murine epitheliums. The RI of the piscine epithelium is significantly higher than its stromal RI and the epithelial RI of the other species, possibly because the piscine eyes function in a water environment as compared to air for the other species. For the three porcine corneas, sample one is from a Yucatan swine while samples two and three are from the domestic Yorkshire swine. The epithelial RI from sample one of the porcine corneas is significantly higher than the epithelial RI from the other two samples which shows that different sub-species could have different RI values. For the other species, the RI values are relatively consistent among the different samples of the same species.

Table 1. Refractive index and thickness results for murine, piscine, human, porcine and bovine corneas

Species	Parameters	Layer		
		L1	L2	Overall
Murine	Refractive Index	1.371 ± 0.016	1.360 ± 0.008	1.362 ± 0.005
	Thickness (μm)	57 ± 18	103 ± 26	160 ± 8
	% of total thickness	36%	64%	100%
Piscine	Refractive Index	1.502 ± 0.057	1.335 ± 0.011	1.360 ± 0.009
	Thickness (μm)	43 ± 1	243 ± 8	286 ± 8
	% of total thickness	15%	85%	100%
Human	Refractive Index	1.433 ± 0.023	1.357 ± 0.013	1.363 ± 0.011
	Thickness (μm)	66 ± 10	760 ± 44	826 ± 49
	% of total thickness	8%	92%	100%
Porcine	Refractive Index	1.476 ± 0.091	1.343 ± 0.013	1.357 ± 0.023
	Thickness (μm)	75 ± 19	809 ± 66	884 ± 51
	% of total thickness	8%	92%	100%
Bovine	Refractive Index	1.400 ± 0.007	1.376 ± 0.003	1.380 ± 0.003
	Thickness (μm)	157 ± 8	843 ± 25	1000 ± 19
	% of total thickness	16%	84%	100%

For each species, the RI and thicknesses of the two distinct layers of the cornea are averaged over multiple samples and the results are summarized in Table 1. For this calculation, the results of 6 murine, 6 piscine, 8 human, 3 porcine, and 5 bovine corneas are averaged for their respective species. Here, the overall RI and thickness are the average RI of the entire cornea (combining L1 and L2) and its corresponding full thickness of the cornea, respectively. The ratios in percentage of the thickness of L1 or L2 to the full corneal thickness are also listed. The RI of L1 and L2 are different across the species likely due to the different cell packing and collagen structures in the epithelium and the stroma, respectively. While the respective RI of L1 and L2 differ greatly across the species, the overall RI appear to be similar around 1.357-1.363 with the exception of the bovine RI which is 1.380. The converging overall RI is caused by the different ratios of the epithelial thickness to the total thickness. For example, murine corneas have the largest ratio of epithelium thickness to total thickness of 36% while the human corneas have the smallest ratio at 8%. The order in ascending thickness is murine, piscine, human, porcine, and then bovine corneas. The relative corneal thicknesses correlate well with the physical sizes of the respective animals.

5. Discussion

Transparency is an important feature of cornea which can be analyzed by the combined MPM/OCT imaging. The corneal transparency is a result of the highly organized collagen packing in the stroma. Swelling disrupts the organized collagen packing and can cause the cornea to have regions of varying RI, which makes the cornea lose its transparency. In the experiment, the human corneas show slight cloudiness due to swelling while the bovine corneas show perfect transparency. In the multimodal imaging, the OCT intensity is directly

#205348 - $15.00 USD Received 28 Jan 2014; revised 30 Mar 2014; accepted 4 Apr 2014; published 14 Apr 2014

proportional to the reflectivity of the tissue under the measurement, while the SHG intensity is affected by the intensity of the excitation light and the collagen structure in the tissue. Assuming that the collagen structure is relatively uniform in the cornea, the SHG intensity thus shows the attenuation of the excitation light.

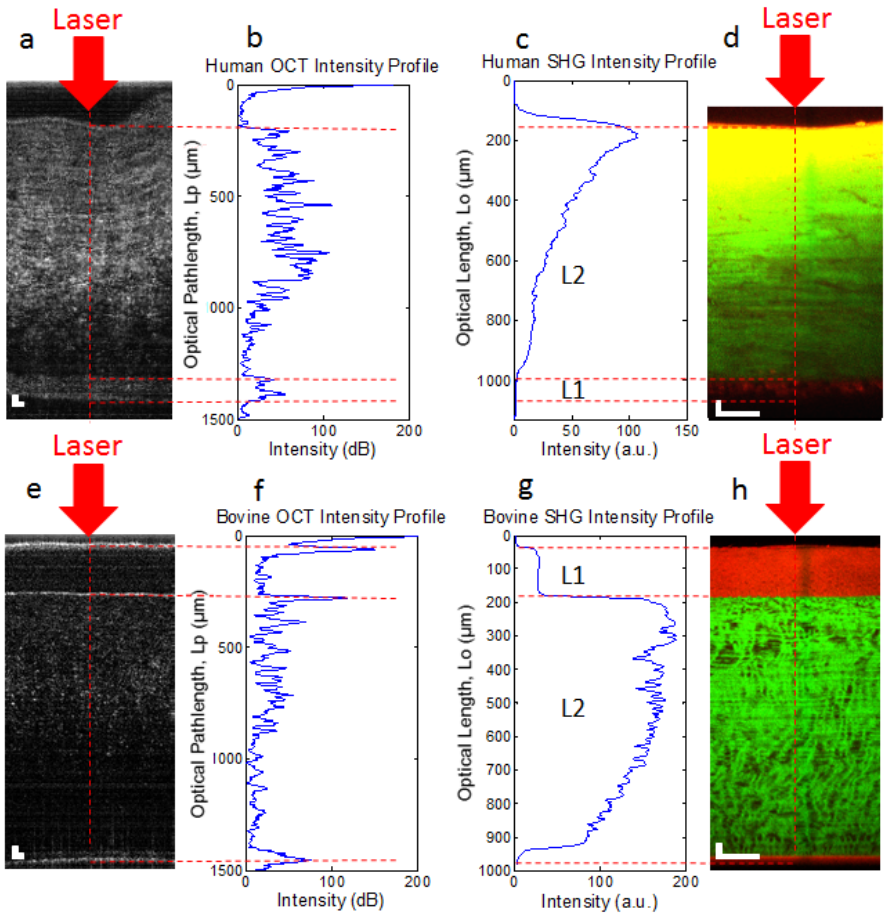

Fig. 10. Comparison between the OCT and SHG signals of a human cornea and a bovine cornea. (a) – (d) OCT image, OCT intensity profile, SHG intensity profile, MPM cross-sectional image of a human cornea, respectively. (e) – (h) OCT image, OCT intensity profile, SHG intensity profile, and MPM cross-sectional image of a bovine cornea, respectively. L1 is the epithelium layer. L2 is the Bowman's layer, stroma, Descemet's membrane, and endothelium layers. Scale bars are 50 μm.

A comparison between the OCT and SHG signal attenuations of a human cornea and a bovine cornea is shown in Fig. 10. The first row (Figs. 10(a)-10(d)) corresponds to the OCT image, the OCT intensity profile, the SHG intensity profile, and the MPM image of a human cornea, respectively. The second row (Figs. 10(e)-10(h)) displays the same information but for a bovine cornea. The red, horizontally-dashed lines mark the anterior epithelial boundary, the epithelium and stroma boundary, and the posterior endothelial boundary. The three boundaries for the bovine cornea are clearly identified as three sharp peaks in the OCT intensity profile in Fig. 10(f). In the SHG intensity profile, Fig. 10(g), the epithelium is shown to have minimal SHG signal. At the junction between the epithelium and the stroma, the SHG signal intensity increases dramatically due to the onset of fibrous collagen. Then it attenuates relatively slowly towards the posterior stroma because the bovine cornea is very transparent. The SHG signal is reduced by 2.29 dB over 750 μm. Meanwhile, in the SHG intensity profile

#205348 - $15.00 USD Received 28 Jan 2014; revised 30 Mar 2014; accepted 4 Apr 2014; published 14 Apr 2014

of the human cornea as shown in Fig. 10(c), because the cornea is imaged from the endothelial side, the SHG intensity increases greatly after the endothelium, due to the collagen in the stroma, and then decreases quickly towards the anterior stroma. The SHG intensity is reduced by 7.96 dB over 750 μm. This is significantly higher than in the bovine case because the human corneal samples exhibit cloudiness and thus scatters the light more. The scattering effect of the cloudy human cornea can also be seen in both the OCT image (Fig. 10(a)) and the OCT intensity profile (Fig. 10(b)) as strong scattering signals in the stroma. The signal in the middle of the stroma is slightly higher because the focus of the objective lens is set in the middle of the stroma. The cloudiness of the human cornea is likely caused by the micro-folds in the stroma from corneal swelling which have been observed in the MPM images. As there are significant scattering from inside the stroma of the human cornea, the scattering from the three boundaries are not as distinct as in the bovine case. In the bovine stroma, dark gaps between the collagenous signals are observed in the MPM images. These dark gaps lack the SHG contrast which indicates that they are not composed of fibrous type-I collagen. Since the OCT image of the bovine cornea shows low scattering and these gaps are not observed, we hypothesize that the gaps have similar RI as the surrounding collagenous material.

In terms of morphology, our study shows that all the five layers of cornea can be observed by the MPM imaging. In the epithelium, larger winged cells are observed at the anterior epithelium and smaller basal cells from the posterior epithelium. The Bowman's layer can be identified as indistinct and diffused signal in the human corneas, and condensed and randomly-arranged layer of fine collagen fiber bundles in the porcine and bovine corneas. However, not every animal species have a Bowman's layer [3]. Hayashi et al. found the Bowman's layer in the C3H mouse to be approximately 0.8 μm [29]. The Bowman's layer is not distinguished in our MPM *en face* images of the mouse likely because it is thinner than the depth resolution of the MPM system. Collin et al. reported that the Bowman's layer was not present in many of the teleost species [3]. The Bowman's layer is not observed in our tilapia samples because tilapia is a type of teleost fish. Morishige et al. observed similar features as in our Figs. 4 and 5 in the human Bowman's layer [26,27]. Merindano et al. reported the existence of the Bowman's layer in bovine corneas but mentioned that it was difficult to distinguish the Bowman's layer in the case of the pig [3]. In our study, a condensed and randomly-arranged layer of finer collagen fiber bundles is observed just posterior to the epithelium of the porcine and bovine corneas, which is attributed as the Bowman's layer for these species.

In the stroma, similarities and differences in the collagen structures across the different species are noticed. The piscine and the human stromata exhibit thin collagen fibers that together seem to indicate an overall collagen direction. In the human corneas, long, straight, and dark ridges are seen that are not present in the other species. These ridges are micro-folds caused by corneal swelling. Murine, porcine, and bovine corneas all exhibit collagen bundles that form interwoven patterns in the stroma. In the porcine and bovine corneas, the interwoven collagen patterns become finer, and denser towards the posterior ends. Similar stromal morphology has been observed by Bueno et al. for the human, porcine, and bovine corneas [14].

The Descemet's membrane and endothelium can be detected by the TPEF contrast which comes from elastin in the Descemet's membrane and NADH from the endothelium. The endothelium is distinguished as the honeycomb cellular structure, while the surrounding region with homogenous TPEF signal is distinguished as the Descemet's membrane in the murine, human and bovine corneas. In the piscine and porcine corneas, the Descemet's membrane and the endothelium could not be differentiated, because their cellular structure is not clear due to the weak signal.

For all the species, higher RI in the epithelium as compared to the stroma is observed. The RI of the two layers vary from species to species possibly due to the different cell packing in the epithelium, and the collagen packing in the stroma. In the literature, the RI of the human epithelium is found to be ~1.397 by Vasudevan et al. and ~1.401 by Patel et al. [23,30], and

#205348 - $15.00 USD Received 28 Jan 2014; revised 30 Mar 2014; accepted 4 Apr 2014; published 14 Apr 2014

the human stromal RI is between ~1.373 to ~1.380 [30]. The overall human corneal RI is found to be in the range of 1.37-1.39 [5,11,17,23]. The RI of the bovine epithelium and the stroma are found to be ~1.376 and ~1.372 respectively [23]. Our RI values fall within reasonable range from these literature results. The human corneas measured in our experiment have a higher thickness than the literature value of ~550 μm [16,22]. The variation is likely from corneal swelling due to the age of the corneas. Nelson et al. found that rabbit and human corneas experienced increased corneal thickness after 3 weeks in the Optisol storage medium [31].

The precision of our RI measurement has been evaluated previously to be within ~1% error compared to reference values on standard samples like water, air, immersion oil, and cover glass [11]. Although our method can have high precision on non-tissue samples, we notice large error bars in some measurements of the corneas. The variations may come from several factors. Firstly, corneal thicknesses and RI are known to change due to fluctuations in the corneal hydration. In literature, the RI of the stromal surface is found to gradually increase exponentially after exposure to air [32]. We also observed as much as a 30% decrease in the piscine corneal thicknesses when exposed to air. We minimized the variations from corneal hydration by submerging all our samples under either BSS sterile irrigation solution or Optisol corneal storage media during the experiment. Furthermore, since all the samples are *ex vivo*, the epithelium and endothelium layers degrade continuously which reduces their ability to maintain corneal hydration. Secondly, there is an inherent sample to sample variation. This can be differences in age, sex, size, and healthy of the sample. Finally, the accuracy of the RI measurement is also affected by the sample thickness where a thinner sample tends to have lower accuracy. Thus the epithelium generally has lower accuracy than the stroma.

For future study, it will be interesting to perform *in vivo* characterization of cornea because there may be morphological and pathological differences between *ex vivo* and *in vivo* tissues. In order to study *in vivo* tissues, several challenges have to be addressed. First, the MPM imaging speed will need to be increased to avoid motion artifacts from subject movements. This requires the implementation of faster scanning methods. Second, as the imaging speed is increased, the image quality will ultimately be limited by the signal to noise ratio. To increase the signal level, the laser power can be increased while keeping it below the safety limit. Alternatively, a laser with a shorter pulse-width can be used to excite TPEF and SHG signals more efficiently.

6. Conclusion

A combined MPM and OCT system is used to image and characterize murine, piscine, human, porcine, and bovine corneas. The five layers of cornea, which are the epithelium, Bowman's layer, stroma, Descemet's membrane, and endothelium, can be distinguished respectively by the high resolution MPM imaging with the TPEF and SHG contrasts from the cells and collagen fibers. The Bowman's layer is observed in the human, porcine, and bovine corneas but not in the murine and piscine corneas. The stroma also shows significantly different collagen structures among the five species. With the co-registered MPM and OCT imaging, the RI and thickness of the two major layers of cornea, the epithelium and stroma, are quantified for the five species. While the overall RI of the entire corneal thickness is similar, the respective RI of the epithelium and stroma vary greatly among the species. Furthermore, the RI of the epithelium is found to be higher than the stroma in all the five species. With the multimodal imaging, a comprehensive analysis of the cornea with both morphological structures and quantitative parameters can be obtained.

Acknowledgments

This work is supported by the British Columbia Innovation Council and the BCFRST Foundation of Canada. We would also like to thank our collaborator at the BC Cancer Agency, Wei Zhang, for providing the murine eyeballs and Christopher Frketich from the Vancouver General Hospital Eye Bank for providing the human corneas.

#205348 - $15.00 USD Received 28 Jan 2014; revised 30 Mar 2014; accepted 4 Apr 2014; published 14 Apr 2014